

Whole-cell 3D STORM reveals interactions between cellular structures with nanometer-scale resolution

Bo Huang^{1,2,4}, Sara A Jones^{2,4}, Boerries Brandenburg^{1,2} & Xiaowei Zhuang^{1–3}

The ability to directly visualize nanoscopic cellular structures and their spatial relationship in all three dimensions will greatly enhance our understanding of molecular processes in cells. Here we demonstrated multicolor three-dimensional (3D) stochastic optical reconstruction microscopy (STORM) as a tool to quantitatively probe cellular structures and their interactions. To facilitate STORM imaging, we generated photoswitchable probes in several distinct colors by covalently linking a photoswitchable cyanine reporter and an activator molecule to assist bioconjugation. We performed 3D localization in conjunction with focal plane scanning and correction for refractive index mismatch to obtain whole-cell images with a spatial resolution of 20–30 nm and 60–70 nm in the lateral and axial dimensions, respectively. Using this approach, we imaged the entire mitochondrial network in fixed monkey kidney BS-C-1 cells, and studied the spatial relationship between mitochondria and microtubules. The 3D STORM images resolved mitochondrial morphologies as well as mitochondria-microtubule contacts that were obscured in conventional fluorescence images.

As a powerful imaging technique for studying cellular processes, fluorescence microscopy allows noninvasive imaging of live samples with molecular specificity. Because of the limited resolution of fluorescence microscopy, however, many biological structures are too small to be observed in detail, prohibiting analyses of molecular interactions within or between these structures. The resolution of light microscopy is classically limited by diffraction to about 200–300 nm in the lateral direction and 500–800 nm in the axial direction; both of these dimensions are substantially larger than the size of many subcellular structures. To overcome this limit, super-resolution optical microscopy approaches have been developed, attaining an order of magnitude improvement in spatial resolution. One category of approaches is based on controlling the spatial pattern of excitation, including stimulated emission depletion (STED) microscopy and its related reversible saturable optical transitions (RESOLFT) technique¹, and saturated structured illumination microscopy (SSIM)². In particular, spatial resolution of about 40–45 nm in three-dimensions has been recently reported using STED³. The other approach is based on single-molecule localization of photoswitchable fluorophores, a

method independently reported under different names including stochastic optical reconstruction microscopy (STORM)⁴, (fluorescence) photoactivation localization microscopy ((f)PALM)^{5,6} and other variants⁷. This approach can generate three-dimensional (3D) super-resolution images by localizing both lateral and axial positions of each photoactivated probe. A lateral resolution of 20–30 nm and an axial resolution of 50–60 nm have been reported using astigmatism imaging, allowing the morphology of nanoscopic cellular structures to be resolved⁸. Similar axial resolutions have been subsequently obtained using bifocal plane imaging⁹.

Although it is important to resolve the 3D morphology of a biological structure, much of biology is governed by interactions between structures. Co-localization analyses with multicolor imaging have been extensively used to map the likelihood of interaction between two components, but the accuracy of co-localization is inherently limited by the image resolution. Structured illumination microscopy has been recently used to image multiple cellular components with a twofold improvement in 3D resolution compared to conventional fluorescence microscopy¹⁰. Substantially higher resolution has been realized in multicolor imaging using two-dimensional (2D) and 3D STED^{3,11}. Multicolor super-resolution imaging has also been previously implemented using STORM/(f)PALM in two dimensions^{12–14}. However, 2D co-localization analyses can be ambiguous considering that biological structures are 3D.

Here we advance STORM/(f)PALM imaging by combining both multicolor and 3D imaging capabilities. To facilitate multicolor imaging, we synthesized probes with distinct colors by covalently linking the photoswitchable cyanine dyes with activator molecules to form a single, functionalized component ready for bioconjugation. To extend beyond previous 3D STORM work on relatively thin samples⁸, we combined focal plane scanning with a new treatment for the spherical aberration induced by refractive index mismatch to image substantially thicker samples and to achieve high-resolution whole-cell imaging. Using these new imaging capabilities, we studied the morphology of the mitochondrial network and the spatial relationship between mitochondria and microtubules in mammalian cells.

¹Howard Hughes Medical Institute, ²Department of Chemistry and Chemical Biology, and ³Department of Physics, Harvard University, 12 Oxford St. Cambridge, Massachusetts 02138, USA. ⁴These authors contributed equally to this work. Correspondence should be addressed to X.Z. (zhuang@chemistry.harvard.edu).

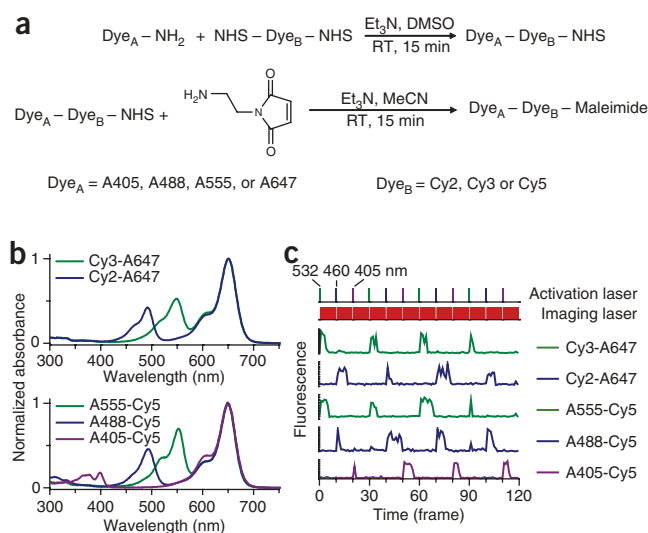


Figure 1 | Synthesis of covalently linked photoswitchable activator-reporter pairs. **(a)** An amine-modified dye (dye_A) and a bis-amine-reactive dye (dye_B) react to form an amine-reactive linked dye pair, which can subsequently convert into a thiol-reactive dye pair through the addition of a maleimide group. Et_3N , triethylamine; DMSO dimethylsulfoxide; MeCN , acetonitrile; RT , room temperature. **(b)** Absorption spectra of linked dye pairs in PBS at pH 7.4. **(c)** Photoswitching traces of linked dye pairs showing that they are specifically activated by light matching the absorption wavelength of the activators. Alternating sequence of green (532 nm), blue (460 nm) and violet (405 nm) activation lasers (top). Between activation pulses, a red (657 nm) laser is used to excite the reporters and to switch them into the dark state (second row). Fluorescence traces of individual probes (bottom five rows).

RESULTS

Synthesis of cyanine-based photoswitchable probes

We have recently reported a family of photoswitchable probes, each composed of a reporter fluorophore that can be switched between a fluorescent and a dark state, and an activator dye that facilitates the reactivation of the reporter from the dark state^{12,15}. Several red or near-infrared cyanine dyes can serve as the reporter. For the activator, there is an even wider array of choices in many distinct colors. Combinatorial pairing of the activators and reporters greatly increases the number of available colors for multicolor imaging. In practice, however, labeling of target molecules with two dyes can be cumbersome. Molecules nonspecifically labeled with activators and reporters often result in heterogeneous populations with distinct switching properties because of different activator-reporter separations. Labeling molecules that contain only a limited number of attachment sites with both reporter and activator can also be difficult. It is, therefore, desirable to connect the activator and reporter into a single chemical unit.

To synthesize covalently linked activator-reporter pairs, we used the procedure depicted in **Figure 1a**. We reacted an amine-modified dye with a dye that contains two amine-reactive *N*-hydroxyl succinimidyl (NHS) ester groups. With an excess of the bis-amine-reactive dye in the reaction, the main product generated was the linked dye-pair with a free NHS ester group, which we then purified using gravity columns or high-performance liquid chromatography. This linked dye-pair can be used for bioconjugation via reaction with primary amines on biomolecules, such as lysine residues on proteins. To broaden the range of labeling targets, we mixed the amine-reactive dye-pair with *N*-(2-aminoethyl) maleimide to create a thiol-reactive dye, which allows coupling with cysteine residues, another commonly used approach for protein labeling. A different scheme has also been used to link Cy3 and Cy5 previously¹⁶.

There are many available choices for both amine-modified dyes and bis-amine-reactive dyes (**Supplementary Fig. 1** online). Bis-amine-reactive forms of most cyanine dyes (Cy2, Cy3, Cy5, Cy5.5 and Cy7) are commercially available; Cy2 and Cy3 can be used as the activator, and Cy5, Cy5.5 and Cy7 can function as the photoswitchable reporter. Many amine-modified dyes, such as Alexa Fluor 405 (A405), Alexa Fluor 488 (A488) and Alexa Fluor 555

(A555), can serve as activators, and the Alexa Fluor 647 (A647), a structural analog of Cy5, can serve as the reporter.

We made five activator-reporter pairs, Cy2-A647, Cy3-A647, A555-Cy5, A488-Cy5 and A405-Cy5, using the procedure described above. The absorption spectra of the purified reaction products exhibited peaks at both activator and reporter absorption wavelengths (**Fig. 1b**). To demonstrate the specific photoswitching ability of the linked dye pairs, we attached them to antibodies and measured fluorescence emission from individual labeled antibody molecules. All of these probes switched to a dark state upon illumination with a red (657 nm) laser, which excites the reporter dyes. Efficient reactivation of the reporters required light that specifically matched the absorption peaks of the activators (**Fig. 1c**). We quantitatively characterized the color specificity of activation, the brightness and the nonspecific activation behavior of these probes as well as how these properties affect super-resolution microscopy (**Supplementary Data** and **Supplementary Fig. 2** online). All of these probes can be used for STORM/(f)PALM imaging. We chose A405-Cy5, A488-Cy5 and A555-Cy5 for our imaging experiments.

Whole-cell 3D imaging

To demonstrate whole-cell 3D STORM, we imaged the entire mitochondrial network in mammalian cells using the covalently linked dye pairs (**Fig. 2**). We used the standard indirect immunological fluorescence method to stain the outer membrane of mitochondria in BS-C-1 cells. We stained Tom20, a component of the translocase of the outer mitochondrial membrane complex and a commonly used mitochondrial outer membrane marker¹⁷, using primary antibodies followed by A405-Cy5-labeled secondary antibodies.

During STORM imaging, we first switched the A405-Cy5 probes to the dark state by the 657 nm laser. Then we used a low-intensity 405 nm activation laser to activate only a small subset of the probes at any given time. This allowed us to resolve individual activated probes and determine their positions with high precision. Then we constructed a super-resolution image by plotting the measured probe positions accumulated over time. To determine the 3D position from the 2D fluorescence image of a probe, we introduced a cylindrical lens in the imaging path to create a focus offset between the two lateral directions, such that not only can the *x* and *y* coordinates of the probe be determined from the center of the image, but the *z* coordinate can also be determined from the ellipticity^{8,18}. To quantify the localization precision, we analyzed the localizations from individual, isolated antibody molecules in the cell sample. The repetitive switching property of the probes

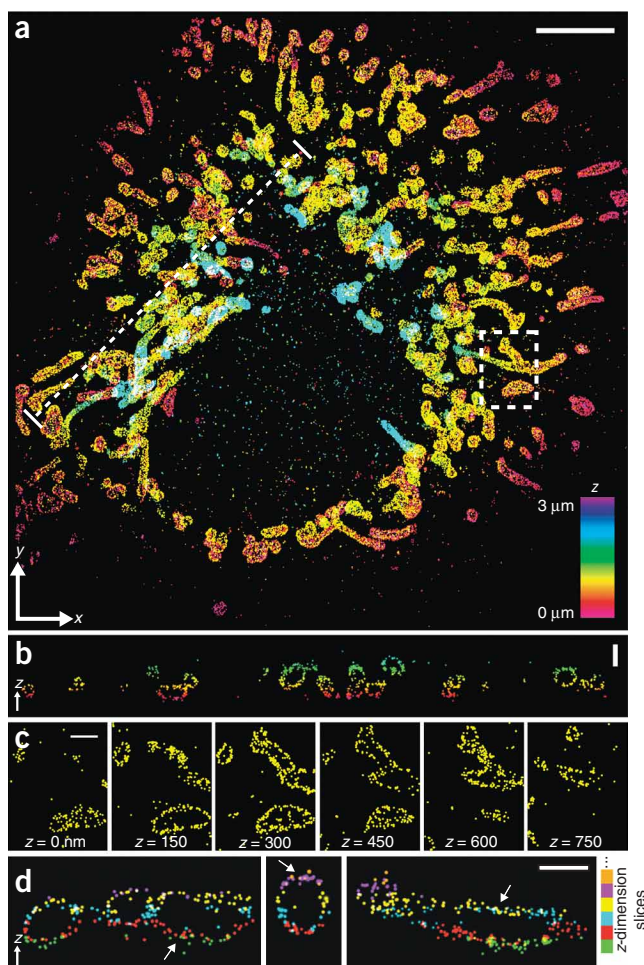


Figure 2 | 3D STORM images of mitochondria in a whole mammalian cell. (a) 3D STORM image of the mitochondrial network in a BS-C-1 cell (see **Supplementary Video 1** for 3D views). The image was acquired in an aqueous medium with refractive index of 1.34. The z-dimension position is color-coded according to the color scale bar. (b) The vertical cross-section along the dotted line in **a**, showing the hollow shape of individual mitochondria. (c) Consecutive x-y sections of the boxed region in **a**. (d) Vertical cross-sections of several regions in **a**, color-coded by the z-dimension slices in which they were originally recorded. Arrows indicate horizontal segments of mitochondria appearing in adjacent z-dimension slices, in which localizations from different slices are colored differently. Six of the nine slices were marked on the right side because the other three do not contain localization points in these sections. Scale bars, 5 μm (**a**), 1 μm (**b,c**); 750 nm (**d**).

second rescaling factor F_2 , which varies with the position of the focal plane (**Supplementary Fig. 3c,d**). The value of F_2 is very close to unity when the focal plane is near the interface, and therefore the effect of spherical aberration can be neglected for imaging a thin sample within several hundred nanometers of the interface⁸. However, when moving away from the interface the value of F_2 for molecules above the focal plane increases rapidly, whereas that below the focal plane remains close to unity (**Supplementary Methods**). Although the average z-dimension position can be corrected by rescaling, the localization precision also rescales with F_2 . Thus, to circumvent the effect of spherical aberration and to ensure the localization precision throughout a thick sample, we chose to accept only localizations below the focal plane.

Alternatively, the spherical aberration can be alleviated using an imaging medium with a higher refractive index. We demonstrated this method using imaging media with a refractive index of 1.45, containing 80% glycerol and 5% glucose or 60% sucrose and 5% glucose (**Supplementary Fig. 4** online). Under these conditions, F_2 was close to unity both below and above the focal plane (**Supplementary Methods** and **Supplementary Fig. 3c,d**), allowing localizations on both sides to be used.

Morphology of the mitochondrial network

The 3D STORM images revealed the hollow shape of the mitochondrial outer membrane that is typically difficult to resolve by conventional wide-field or confocal fluorescence microscopy (**Fig. 2**). The mitochondrial outer membrane appeared as a thin envelope that enclosed a hollow space, in which the mitochondrial inner membrane and matrix presumably reside (**Fig. 2b,c** and **Supplementary Video 1** online). Such a hollow structure also had been previously resolved using 3D STED³. Some mitochondria span multiple z-dimension slices, allowing us to estimate the accuracy of our methods for combating spherical aberration by examining how well the same cellular structures that appeared in adjacent z-dimension slices align with each other (**Fig. 2d**). By comparing the same horizontal segments of mitochondria that appeared in both slices, we measured the discrepancy between the independently determined z-dimension positions in the adjacent slices. The discrepancy was 18 nm on average, well within our axial resolution of 60–70 nm.

The whole-cell images also revealed two distinct types of mitochondrial morphology: mitochondria appeared globular and dispersed in some cells, and as a tubular and interconnected network in others (**Fig. 2** and **Supplementary Fig. 4**). We observed both types of morphology using all imaging buffers mentioned above, as

allowed each molecule to be localized multiple times, and the dispersion of the localizations, 25 nm in x and y , and 67 nm in z (full width at half maximum values), provided a measure of the average localization precision within a 600 nm depth near the focal plane⁸. The localization precision degrades when the molecule is further away from the focal plane, limiting the z-dimension imaging range if the position of the focal plane is fixed. To image the full depth of a mammalian cell, typically several micrometers thick, we scanned the axial position of the objective to acquire multiple image slices at focal planes deeper into the cell. Then we stacked these slices to form whole-cell 3D images that were $\sim 50 \mu\text{m}$ wide and $\sim 3 \mu\text{m}$ thick.

For 3D imaging of an aqueous sample using an oil immersion objective, the difference in refractive index between the imaging medium and the coverglass-oil-objective system must be considered (**Supplementary Methods** online). This refractive index mismatch causes the light rays to bend when passing across the medium-coverglass interface, effectively increasing the apparent z-dimension position of the molecule (**Supplementary Fig. 3a,b** online). When the image depth is not too large, this effect can be corrected by a linear rescaling factor F close to unity as shown in the previous confocal and 3D STORM work^{8,19}. The refractive index mismatch also causes spherical aberration because the refracted light rays no longer converge perfectly, distorting the point spread function and making it asymmetric in the axial direction. Simulations revealed that this effect can be quantitatively described by a

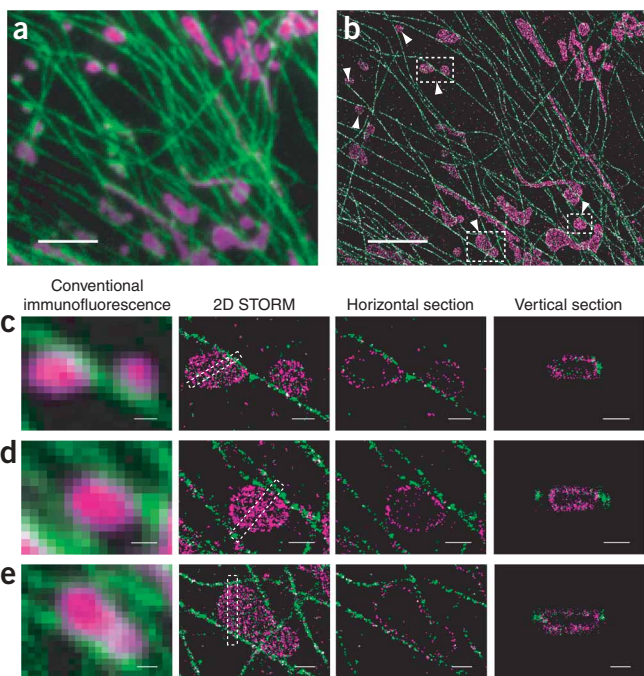


Figure 3 | Two-color 3D STORM images of mitochondria and microtubules. **(a)** A conventional fluorescence image of mitochondria (magenta) and microtubules (green) normalized over excitation laser intensities. **(b)** STORM image of the same area with all localizations at different z-dimension positions stacked. The image was acquired in aqueous medium and reconstructed from 500,000 localization points. It contains one 650-nm-thick image slice. **(c–e)** Magnified views of the boxed regions in **b**. The conventional fluorescence image, the 2D STORM image, a horizontal cross-section and the vertical cross-section of the boxed region in the 2D STORM image are shown. See **Supplementary Video 2** online for a 3D rendering of **e**. Scale bars, 3 μm (**a,b**) 500 nm (**c–e**).

localizations were colored according to the corresponding activation laser immediately preceding the activation events.

The STORM image clearly resolved mitochondria and microtubules even when they were densely packed, allowing a more precise determination of their spatial relation as compared to the conventional fluorescence image (**Figs. 3a,b**). The globular mitochondria (**Figs. 3c,d**) often contacted microtubules, consistent with transport of mitochondria observed on microtubules^{24,25}. However, we also observed many false contacts between mitochondria and microtubules in the conventional fluorescence image. For example, one mitochondrion appeared to touch two microtubules on both sides in the conventional image, whereas the STORM image clearly revealed a 150 nm separation from the left microtubule and a close contact site to the microtubule on the right (**Fig. 3d**). We often observed mitochondria to be surrounded by microtubules (**Fig. 3e** and **Supplementary Video 2** online).

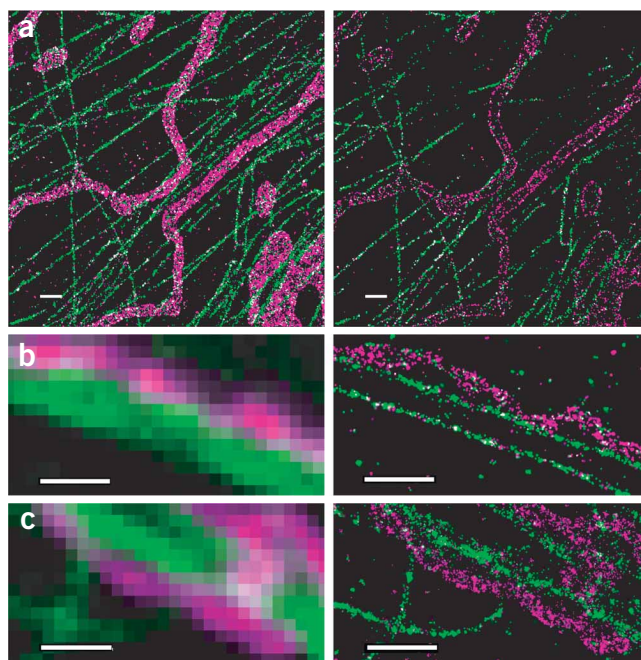
Spatial relations of the tubular mitochondria and microtubules were more complex. Although some mitochondrial tubes aligned along the microtubules, others did not (**Fig. 4** and **Supplementary Fig. 5** online). Some tubular mitochondria that appeared to lie on microtubules revealed noncontiguous interaction, with contact points separated by stretches of noncontact regions in a way similar to inchworms (**Fig. 4b,c**). Such a spatial relationship was again obscured in the conventional fluorescence images.

well as different fixation methods and cell types. The distinctive morphologies likely indicate cells in different growth stages as has been demonstrated previously^{20,21}: the interconnected tubular network of mitochondria present during interphase disintegrates during the mitotic phase²² and during apoptosis²³. The super-resolution images also allowed us to quantify the size of individual mitochondria. Whereas the globular type of mitochondria were relatively dispersed in size, ranging from 200 to 1,500 nm, the diameter for the tubular structures was much more uniform, with a narrow distribution of 210 ± 10 nm in B-SC-1 cells. What regulates the width of the tubular mitochondria is currently unknown.

Multicolor 3D imaging of mitochondria and microtubules

To maintain a dynamic morphology, mitochondria in a living cell are constantly transported and reorganized by motor proteins attached to the cytoskeleton, especially microtubules in mammalian cells^{24,25}. To map their spatial relation, we performed two-color 3D STORM by staining Tom20 and β -tubulin. We used A405-Cy5-labeled secondary antibodies for detecting mitochondria and A555-Cy5- or A488-Cy5-labeled secondary antibodies to stain the microtubules. During image acquisition, we used an alternating sequence of 405-nm and 532-nm (or 460-nm) laser pulses to activate A405-Cy5 and A555-Cy5 (or A488-Cy5) probes, respectively. Then we imaged the activated probes by the 657 nm laser in between the activation pulses to determine their 3D positions. The

Figure 4 | Two-color STORM images showing interactions between tubular mitochondria (magenta) and microtubules (green) in three BS-C-1 cells. **(a–c)** The imaging conditions are identical to those described in **Figure 3**. Images shown here are magnified views of the boxed regions of the large-field images shown in **Supplementary Figure 5** online. **(a)** Comparison of the z-stacked STORM image (left) and a 100 nm thick horizontal section displaying hollow tubes of mitochondria (right). **(b,c)** Inchworm-like interactions between tubular mitochondria and microtubules in two different cells are resolved in STORM images (right) but not in conventional fluorescence images (left). Scale bars, 1 μm .



Though the importance of this inchworm-like contact mode is unclear, we speculate that it might make it easier to transport mitochondria, as mitochondria-microtubule contacts are often mediated by motor proteins²⁵. These observations can be extended to include motor proteins, fusion- and fission-related proteins, as well as other cytoskeletal structures, to study how the morphology of mitochondria is regulated in cells^{21,24–26}.

DISCUSSION

The multicolor 3D super-resolution optical imaging capabilities shown here allow quantitative and nanometer-scale examination of specific molecular interactions, which is often difficult to obtain using other high-resolution imaging methods such as electron microscopy owing to the low labeling efficiency of biomolecules with electron-dense tags, such as immunogold. Accurate measurement of molecular structures and interactions requires a proper understanding of the factors that affect the 3D image resolution. For thick-sample imaging, the refractive index mismatch between the imaging media and the objective-coverglass system may alter the axial resolution. A high-numerical-aperture oil immersion objective provides high photon collection efficiency and a tight focus, both beneficial for the localization precision. However, when used to image an aqueous sample, such as cells in a physiological buffer, the observed axial position of a molecule needs to be corrected for the refractive-index mismatch^{8,19}. Moreover, the index mismatch also results in spherical aberration that can substantially reduce the *z*-dimension localization precision for molecules above the imaging focal plane when they are sufficiently far away from the sample-coverglass interface. Notably, we found that spherical aberration exerted only a minimal effect on the localization precision of molecules below the imaging focal plane, providing a means to maintain high localization precision for at least several micrometers into the sample. Alternatively, index-matching media may also be used to reduce the spherical aberration for oil immersion objectives, although they are typically not compatible with live-cell imaging. Water immersion objectives nearly eliminate spherical aberration for aqueous samples, but the lower photocollection efficiency and less tight focus owing to a smaller numerical aperture are unfavorable for high localization precision.

The effective resolution for resolving cellular structures not only depends on the intrinsic optical resolution but also on the label size and density. For imaging mitochondria and microtubules, we chose the commonly used immunological fluorescence method, in which the size of the label, namely the primary and secondary antibodies, is ~ 10 nm. The label densities achieved here were such that the average distance between neighboring tubulin labels was ~ 20 nm and that between Tom20 labels was ~ 70 nm. In addition, a sample preparation procedure that preserves the ultrastructure of the cellular components is also crucial for maintaining a high effective resolution. For example, compared to the fixation and staining methods used in this work (**Supplementary Methods**), suboptimal fixation methods tend to break cytoskeletal structures and stronger permeabilization reagents tend to lower the labeling density of membrane proteins (**Supplementary Fig. 6** online).

Finally, additional improvement in resolution is possible considering the brightness of photoswitchable cyanine dyes. The $\sim 5,000$ photons detected from these dyes per switching cycle allows, in principle, localization precision of several nanometers,

assuming that the flexible linkers between the dye and the target protein allow it to freely rotate and be treated as an isotropic emitter²⁷. The covalently linked activator-reporter pairs that we created here allow the probes to be linked directly to specific sites of target proteins. For example, the linked dye can be coupled to an enzymatic substrate, which can then be ligated to a specific peptide sequence fused to a protein of interest, allowing genetic targeting of these bright photoswitchable probes^{28–30}. Such a direct linkage of a small photoswitchable probe to a target protein can additionally increase label density and reduce label size, as compared to larger labels such as antibodies and fluorescent proteins. Combination of this genetic targeting strategy with the high localization precision afforded by these bright probes promises molecular-scale resolution in future fluorescence imaging.

METHODS

Synthesis of covalently linked activator-reporter pairs. Cy2, Cy3 and Cy5 bis NHS ester were purchased from GE Healthcare. A405, A488, A555 and A647 cadaverines were from Invitrogen. To synthesize an amine-reactive activator-reporter pair, the selected cadaverine-modified Alexa Fluor dye and bis NHS cyanine dye were dissolved in anhydrous dimethyl sulfoxide (DMSO) at a concentration of 5 mg ml^{-1} and subsequently mixed in a 1:3 molar ratio. Fourfold molar equivalent of triethylamine was then added to the reaction mix, and the reaction was carried out for 15 min at room temperature (22°C). The product was purified on a C_{18} gravity column equilibrated with acetonitrile and eluted with 1:2 acetonitrile:dimethyl formamide. The product eluted off the column in the first colored fraction. Alternatively, the product was purified by high-performance liquid chromatography using a C_{18} column and eluted with an acetonitrile-water gradient in triethylamine-acetic acid buffer at pH 7.5.

To prepare thiol-reactive dyes, the amine-reactive activator-reporter pair eluted from the gravity column was mixed with a fourfold molar equivalent of *N*-aminoethyl maleimide (Sigma-Aldrich) and triethylamine. The reaction was carried out for 15 min at room temperature. The product was precipitated by adding equal volume of ethyl acetate, dissolved in DMSO and then purified using a C_{18} column.

STORM imaging. BS-C-1 cells (American Type Culture Collection) were fixed, immunostained with rabbit anti-Tom20 (Santa Cruz Biotech) and/or mouse anti- β -tubulin (TUB2.1; Cytoskeleton). The stained cells were imaged in PBS with the addition of 100 mM mercaptoethylamine at pH 8.5, 5% glucose (wt/vol) and oxygen scavenging enzymes (0.5 mg ml^{-1} glucose oxidase (Sigma-Aldrich), and $40 \text{ } \mu\text{g ml}^{-1}$ catalase (Roche Applied Science)), unless otherwise mentioned. This above imaging buffer has a refractive index of 1.34. Media with higher refractive index (1.45) containing 80% (vol/vol) glycerol and 5% (wt/vol) glucose, or 60% (wt/wt) sucrose solution and 5% (wt/wt) glucose, were used in some experiments, both with the same amount of mercaptoethylamine and oxygen scavenging enzymes as described above. The slight mismatch between the medium refractive index and coverglass was needed for focus locking during imaging. Although a high concentration of mercaptoethylamine and oxygen scavenging system were used here for fixed cell imaging, the cyanine dyes also switch in buffers with lower concentrations of thiol and oxygen scavenger system compatible with live-cell imaging¹².

For 3D imaging, a cylindrical lens with a focal length of 1 m was inserted into the imaging optical path for 3D localization⁸. To stabilize the microscope focusing during data acquisition, the reflected excitation laser from the coverglass-medium interface was directed to a quadrant photodiode. The position read out of the quadrant photodiode, which was sensitive to the distance between the coverglass and the objective focal plane, was used to provide feedback to a piezo objective positioner (Nano-F100; MadCity Labs), allowing compensation for the focus drift. The residual drift, < 40 nm (Supplementary Fig. 7 online), was corrected during data analysis. For whole-cell imaging in an aqueous medium, the objective positioner was stepped in 300 nm intervals, which corresponds to a focal plane displacement of 216 nm after correcting for the refractive index mismatch at the glass-medium interface. Molecules within 270 nm below the focal plane were accepted for image reconstruction. Whole-cell images were obtained from 9 partially overlapped z-dimension slices. For imaging in media with a refractive index of 1.45, the positioner was stepped in 650 nm intervals, corresponding to an actual focal plane displacement of 580 nm. Molecules within 360 nm above and below the focal plane were accepted and whole-cell images were obtained from four partially overlapped z-dimension slices.

For single-color imaging, the A405-Cy5 labeled sample was continuously illuminated with a 657 nm imaging laser (~30 mW). A low intensity 405 nm laser was used to activate the probes, with intensity adjusted such that only an optically resolved subset of the probes were activated at any given time. In certain cases, the 405 nm laser could be omitted because the 657 nm laser can also activate Cy5, albeit at a low rate. Emission from the fluorophores were recorded by the camera at a frame rate of 20 Hz. We performed 3D localization of individual molecules as described previously⁸. Multicolor imaging was performed by illuminating the sample repetitively with each frame of an activation laser followed by three frames of the 657 nm imaging laser. An alternating sequence of two activation lasers was used for two-color imaging. The 405 nm, 460 nm and 532 nm lasers were used to activate A405-Cy5, A488-Cy5 and A555-Cy5, respectively.

Additional methods. Descriptions of the immunostaining conditions, microscope setup and data analysis procedure including the correction to the refractive index mismatch are available in **Supplementary Methods**.

Note: Supplementary information is available on the Nature Methods website.

ACKNOWLEDGMENTS

This work is supported by in part by the US National Institutes of Health (to X.Z.). X.Z. is a Howard Hughes Medical Institute Investigator.

Published online at <http://www.nature.com/naturemethods/>
Reprints and permissions information is available online at
<http://npg.nature.com/reprintsandpermissions/>

- Hell, S.W. Far-field optical nanoscopy. *Science* **316**, 1153–1158 (2007).
- Gustafsson, M.G.L. Nonlinear structured-illumination microscopy: wide-field fluorescence imaging with theoretically unlimited resolution. *Proc. Natl. Acad. Sci. USA* **102**, 13081–13086 (2005).
- Schmidt, R. *et al.* Spherical nanosized focal spot unravels the interior of cells. *Nat. Methods* **5**, 539–544 (2008).
- Rust, M.J., Bates, M. & Zhuang, X.W. Sub-diffraction-limit imaging by stochastic optical reconstruction microscopy (STORM). *Nat. Methods* **3**, 793–795 (2006).
- Betzig, E. *et al.* Imaging intracellular fluorescent proteins at nanometer resolution. *Science* **313**, 1642–1645 (2006).
- Hess, S.T., Girirajan, T.P.K. & Mason, M.D. Ultra-high resolution imaging by fluorescence photoactivation localization microscopy. *Biophys. J.* **91**, 4258–4272 (2006).
- Egner, A. *et al.* Fluorescence nanoscopy in whole cells by asynchronous localization of photoswitching emitters. *Biophys. J.* **93**, 3285–3290 (2007).
- Huang, B., Wang, W.Q., Bates, M. & Zhuang, X.W. Three-dimensional super-resolution imaging by stochastic optical reconstruction microscopy. *Science* **319**, 810–813 (2008).
- Juette, M.F. *et al.* Three-dimensional sub-100 nm resolution fluorescence microscopy of thick samples. *Nat. Methods* **5**, 527–529 (2008).
- Schemmelleh, L. *et al.* Subdiffraction multicolor imaging of the nuclear periphery with 3D structured illumination microscopy. *Science* **320**, 1332–1336 (2008).
- Donnert, G. *et al.* Two-color far-field fluorescence nanoscopy. *Biophys. J.* **92**, L67–L69 (2007).
- Bates, M., Blosser, T.R. & Zhuang, X.W. Multicolor super-resolution imaging with photo-switchable fluorescent probes. *Science* **317**, 1749–1753 (2007).
- Bock, H. *et al.* Two-color far-field fluorescence nanoscopy based on photoswitchable emitters. *Appl. Phys. B-Lasers Opt.* **88**, 161–165 (2007).
- Shroff, H. *et al.* Dual-color superresolution imaging of genetically expressed probes within individual adhesion complexes. *Proc. Natl. Acad. Sci. USA* **104**, 20308–20313 (2007).
- Bates, M., Blosser, T.R. & Zhuang, X.W. Short-range spectroscopic ruler based on a single-molecule optical switch. *Phys. Rev. Lett.* **94**, 108101 (2005).
- Conley, N.R., Biteen, J.S. & Moerner, W.E. Cy3-Cy5 covalent heterodimers for single-molecule photoswitching. *J. Phys. Chem. B* **112**, 11878–11880 (2008).
- Neupert, W. & Herrmann, J.M. Translocation of proteins into mitochondria. *Annu. Rev. Biochem.* **76**, 723–749 (2007).
- Kao, H.P. & Verkman, A.S. Tracking of single fluorescent particles in 3 dimensions - use of cylindrical optics to encode particle position. *Biophys. J.* **67**, 1291–1300 (1994).
- Hell, S., Reiner, G., Cremer, C. & Stelzer, E.H.K. Aberrations in confocal fluorescence microscopy induced by mismatches in refractive-index. *J. Microsc.* **169**, 391–405 (1993).
- Chan, D.C. Mitochondria: Dynamic organelles in disease, aging, and development. *Cell* **125**, 1241–1252 (2006).
- Frazier, A.E., Kiu, C., Stojanovski, D., Hoogenraad, N.J. & Ryan, M.T. Mitochondrial morphology and distribution in mammalian cells. *Biol. Chem.* **387**, 1551–1558 (2006).
- Taguchi, N., Ishihara, N., Jofuku, A., Oka, T. & Mihara, K. Mitotic phosphorylation of dynamin-related GTPase Drp1 participates in mitochondrial fission. *J. Biol. Chem.* **282**, 11521–11529 (2007).
- Gao, W., Pu, Y., Luo, K.Q. & Chang, D.C. Temporal relationship between cytochrome c release and mitochondrial swelling during UV-induced apoptosis in living HeLa cells. *J. Cell Sci.* **114**, 2855–2862 (2001).
- Anesti, V. & Scorrano, L. The relationship between mitochondrial shape and function and the cytoskeleton. *Biochim. Biophys. Acta-Bioenerg.* **1757**, 692–699 (2006).
- Boldogh, I.R. & Pon, L.A. Mitochondria on the move. *Trends Cell Biol.* **17**, 502–510 (2007).
- Frederick, R.L. & Shaw, J.M. Moving mitochondria: Establishing distribution of an essential organelle. *Traffic* **8**, 1668–1675 (2007).
- Enderlein, J., Toprak, E. & Selvin, P.R. Polarization effect on position accuracy of fluorophore localization. *Opt. Express* **14**, 8111–8120 (2006).
- Chen, I., Howarth, M., Lin, W.Y. & Ting, A.Y. Site-specific labeling of cell surface proteins with biophysical probes using biotin ligase. *Nat. Methods* **2**, 99–104 (2005).
- Fernandez-Suarez, M. *et al.* Redirecting lipoyl acid ligase for cell surface protein labeling with small-molecule probes. *Nat. Biotechnol.* **25**, 1483–1487 (2007).
- Popp, M.W., Antos, J.M., Grotenbreg, G.M., Spooner, E. & Ploegh, H.L. Sortagging: a versatile method for protein labeling. *Nat. Chem. Biol.* **3**, 707–708 (2007).